Supplementary Information

Negative to Positive Axial Thermal Expansion Switching of an Organic Crystal: Contribution to Multistep Photoactuation

Shodai Hasebe,[‡1] Yuki Hagiwara,[‡1] Takashi Ueno,[2] Toru Asahi,[1,2,3] and Hideko Koshima[*3]

[1] Department of Advanced Science and Engineering, Graduate School of Advanced Science and Engineering, Waseda University, Tokyo 169-8555, Japan

[2] Department of Nanoscience and Nanoengineering, Graduate School of Advanced Science and Engineering, Waseda University, Tokyo 169-8555, Japan

[3] Research Organization for Nano and Life Innovation, Waseda University, Tokyo 162-0041, Japan

[‡] These authors contributed equally to this work.

* Correspondence to h.koshima@kurenai.waseda.jp

Contents

1. Experimental Method

Materials

N-3,5-di-*tert*-butylsalicylide-3-nitroaniline enol-**1** was synthesized through the condensation of aldehyde and aniline; 3,5-di-*tert*-butylsalicylaldehyde (5 mmol) and 3-nitroaniline (5 mmol) were dissolved in 2-propanol (15 mL), added to a vial tube, and heated by microwave (Monowave 300, Anton Paar, Graz, Austria) for two hours at 150°C. Single crystals of enol-**1** were prepared by slow evaporation of a methanol solution at ambient temperatures under atmosphere pressure. Thin microcrystals of enol-**1** were obtained by sublimation; single bulk enol-**1** crystals were put in a glass Petri dish covered with a glass slide on which sublimed microcrystals were crystallized. The Petri dish was heated on a heater for several days at 110–120°C.

Thermal analysis

Differential scanning calorimetry (DSC) profiles measurements were conducted using a differential scanning calorimeter (DSC 8500, PerkinElmer, Waltham, MA, USA) at a heating and cooling rate of 10°C min^{-1} for a temperature range from 0 to 100°C under nitrogen gas at atmospheric pressure. The specific heat capacity of the enol-**1** crystal was determined against the aluminium oxide standard by the calorimeter mentioned above according to the following equation:

$$Cp_s = {}^{h_s m_r Cp_r}/_{h_r m_s}$$

where *Cp*, *h*, and *m* represent the specific heat capacity, the heat flow difference based on the empty cell, and the sample weight, respectively. The subscripts of *s* and *r* represent the enol-**1** crystal (sample) and the aluminium oxide standard (reference), respectively. The specific heat capacity of the aluminium oxide standard Cp_r was referenced to the Network Database System for Thermophysical Property Data of The National Institute of Advanced Industrial Science and Technology (AIST).[S1]

Single-crystal X-ray diffraction analysis

Single-crystal X-ray diffraction data were collected using an R-AXIS RAPID-II Imaging plate camera (Rigaku Corp., Tokyo, Japan) with Cu Kα radiation (λ= 1.54186 Å). The temperature of the sample was controlled using a nitrogen gas flow cryostat and the temperature was calibrated with a thermocouple. The initial structures were solved by employing direct methods in the SHELXT program[S2] and refined on F^2 using full-matrix least-squares techniques in the SHELXL program.[S3] Calculations were performed using the Rigaku CrystalStructure software package (Rigaku)[S4] and the Olex2 graphical interface.[S5]

Energy framework analysis

Energy framework analysis was conducted by using CrystalExplorer[S6] on Windows 10. The total intermolecular interaction energies were calculated based on Gaussian B3LYP-D2/6-31G(d,p) molecular wavefunctions.

Ultraviolet-visible diffuse reflectance spectra measurement

Ultraviolet–visible (UV–vis) diffuse reflectance spectra of powdered enol-**1** crystals were measured using a spectrometer (Lambda 650; PerkinElmer). Powdered crystals were mounted on a glass plate, covered with a quartz glass plate, and then irradiated with a UV laser (375 nm, UV-400, FOLS-03, Sawaki Kobo, Shizuoka, Japan) to determine its photoisomerisation properties. After the spectral change became saturated, the UV light was turned off and the sample was irradiated with visible light (520 nm, FOLS-03, Sawaki Kobo) to clarify its photochemical back-isomerization properties.

Mechanical bending observations

The mechanical bending of enol-**1** crystals under UV light irradiation was recorded using a digital high-speed microscope at a frame rate of 30–1000 fps (VW-6000, Keyence, Osaka, Japan). Irradiation was conducted using UV and visible light lasers (375 and 520 nm, respectively; FOLS-03, Sawaki Kobo) or UV-LED (365 nm, UV-400, Keyence). The output laser beam was collimated using a collimator (F220FC-532, Thorlabs Inc., Newton, NJ, USA). Light irradiation was controlled manually or using a microcontroller (UNO; Arduino, Somerville, MA, USA). Movies were analysed using the Tracker Video Analysis and Modelling Tool[S7] to extract the time dependence of the bend angle of the crystal tip. Surface temperature distribution changes upon irradiation with light were monitored using an infrared thermography camera at a frame rate of 20–60 fps (FSV-2000, Apiste, Osaka, Japan). All measurements were conducted at room temperature (20–25 ℃) unless otherwise mentioned. Measurement above 30℃ was carried out by heating the entire crystal with a halogen heater (HPH-12/f6/12v-20w, Heat-tech Co., Ltd., Kobe, Japan).

2. Characterisation

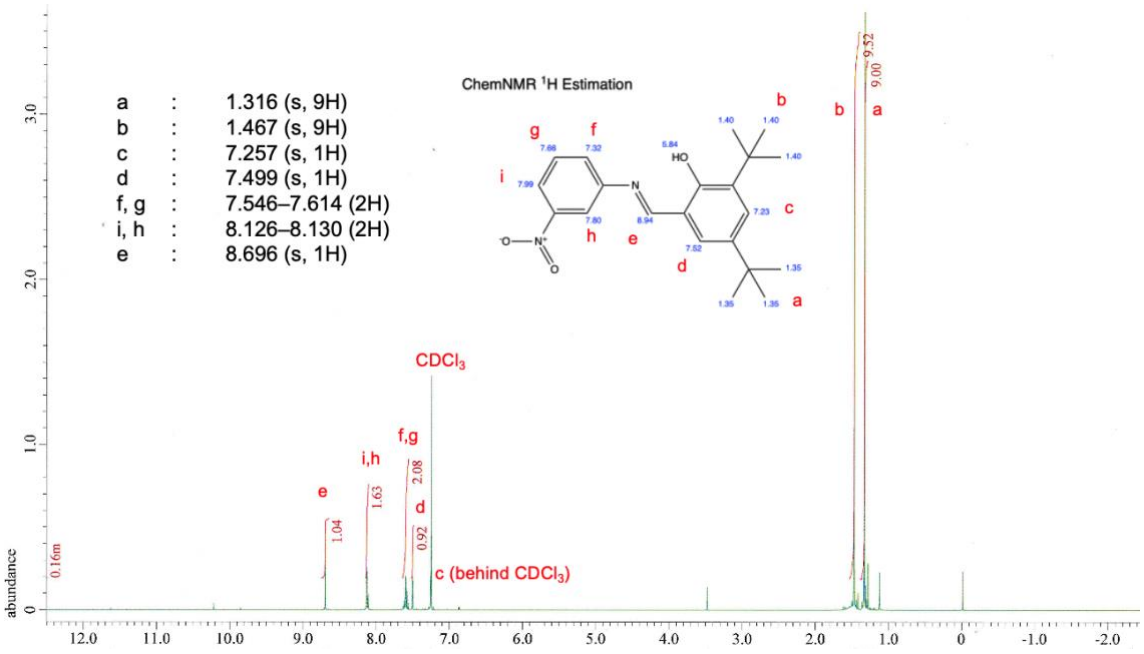

Fig. S1 ^{1}H NMR spectrum of enol-**1** (500 MHz, $CDCl_3$).

Note: The peak of the hydroxy group (Ph-OH) appears at 13.1 ppm.[S8]

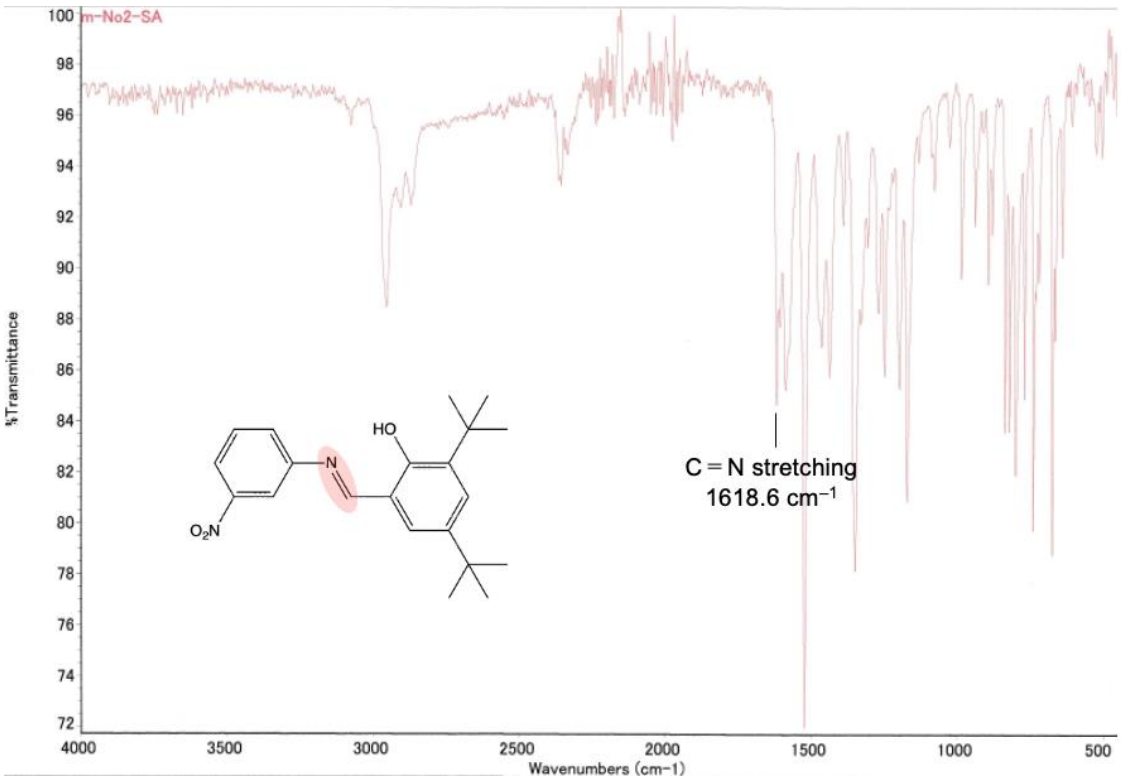

Fig. S2 IR spectrum of powder enol-**1** crystals.

Note: Enol-**1** has a strong C=N stretching peak at 1622 cm^{-1}.[S8]

3. Thermal analysis

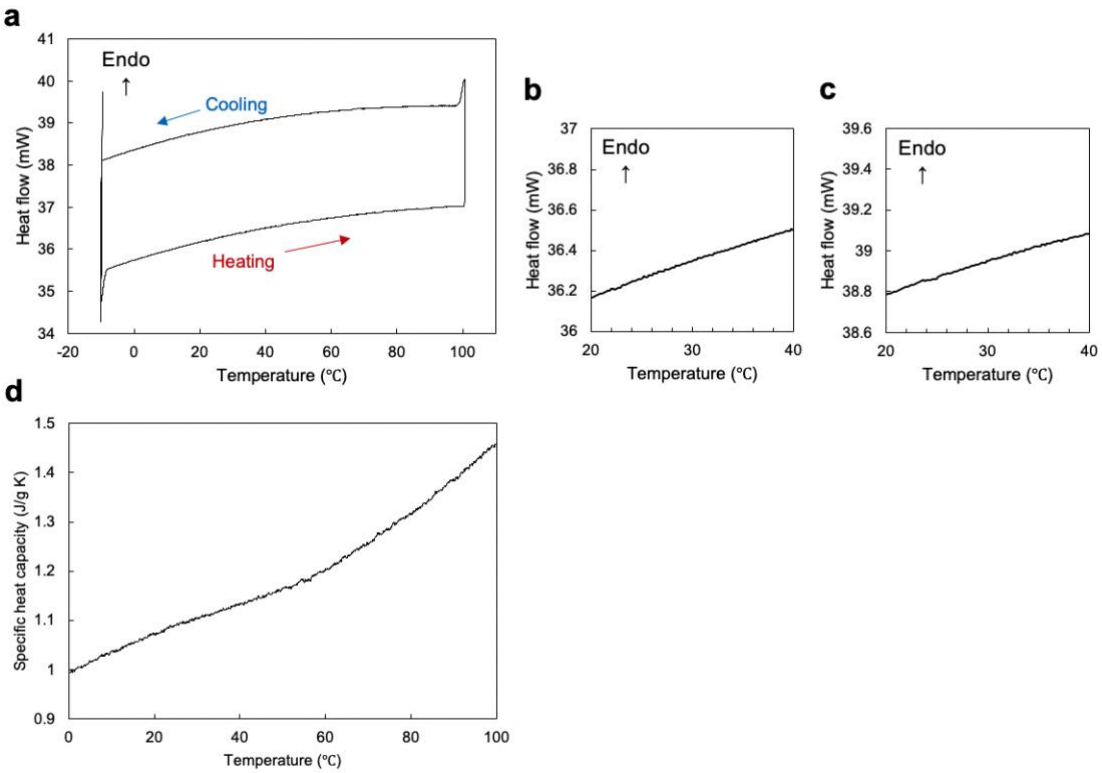

Fig. S3 (a) Differential scanning calorimetry (DSC) curve of enol-**1** crystals upon heating and cooling from –10 to 100 ℃ and (b, c) enlarge views upon (b) heating and (c) cooling. (d) Specific heat capacity of enol-**1** crystals. No peaks by thermal phase transitions were confirmed.

4. Crystal structures

Table S1 Unit cell parameters of the enol-**1** crystal at different temperatures.

Temperature/°C	–1.6	6.8	15.2	23.6
Formula	$C_{21}H_{26}N_2O_3$	$C_{21}H_{26}N_2O_3$	$C_{21}H_{26}N_2O_3$	$C_{21}H_{26}N_2O_3$
Crystal system	Triclinic	Triclinic	Triclinic	Triclinic
Space group	$P\bar{1}$	$P\bar{1}$	$P\bar{1}$	$P\bar{1}$
a/Å	6.0499(6)	6.0455(6)	6.0419(6)	6.0399(7)
b/Å	10.3177(9)	10.3195(10)	10.3191(11)	10.3202(11)
c/Å	16.6641(15)	16.7114(17)	16.7479(18)	16.7772(18)
α/°	101.437(7)	101.333(7)	101.248(7)	101.178(7)
β/°	92.135(6)	92.155(6)	92.177(6)	92.181(6)
γ/°	101.786(7)	101.650(7)	101.546(7)	101.469(7)
Z	2	2	2	2
V/Å^3	994.76(16)	997.93(18)	1000.17(18)	1002.25(19)
d_{calc}/g cm^{-3}	1.183	1.180	1.177	1.174
R_1 [$I>2\sigma(I)$]	0.072	0.0738	0.0745	0.0797
wR_2 [$I>2\sigma(I)$]	0.1885	0.1973	0.1950	0.2019
GOF	1.100	1.107	1.086	1.149

Temperature/°C	32.0	40.4	48.8	57.2
Formula	$C_{21}H_{26}N_2O_3$	$C_{21}H_{26}N_2O_3$	$C_{21}H_{26}N_2O_3$	$C_{21}H_{26}N_2O_3$
Crystal system	Triclinic	Triclinic	Triclinic	Triclinic
Space group	$P\bar{1}$	$P\bar{1}$	$P\bar{1}$	$P\bar{1}$
a/Å	6.0394(8)	6.0405(8)	6.0445(9)	6.0467(10)
b/Å	10.3207(13)	10.3230(13)	10.3300(14)	10.3324(17)
c/Å	16.801(2)	16.826(2)	16.853(2)	16.871(3)
α/°	101.124(7)	101.079(7)	101.035(7)	101.000(7)
β/°	92.180(6)	92.174(6)	92.153(6)	92.143(6)
γ/°	101.408(7)	101.364(7)	101.338(7)	101.307(7)
Z	2	2	2	2
V/Å^3	1004.1(2)	1006.3(2)	1009.6(3)	1011.5(3)
d_{calc}/g cm^{-3}	1.172	1.170	1.166	1.164
R_1 [$I>2\sigma(I)$]	0.0802	0.0823	0.0861	0.0865
wR_2 [$I>2\sigma(I)$]	0.2133	0.2249	0.2458	0.2395
GOF	1.120	1.094	1.094	1.080

a

Temperature/°C	-1.6	6.8	15.2	23.6	32.0	40.4	48.8	57.2
① N=C /Å	1.281(4)	1.281(4)	1.280(4)	1.280(4)	1.280(4)	1.279(4)	1.279(4)	1.280(4)
② O–C /Å	1.357(3)	1.357(4)	1.357(4)	1.356(4)	1.359(4)	1.359(4)	1.359(4)	1.361(4)
③ O–H---N /Å	1.864	1.867	1.864	1.863	1.862	1.864	1.867	1.877
③ O---N /Å	2.600	2.601	2.602	2.601	2.600	2.602	2.605	2.606
Dihedral angle between salicyl and phenyl rings /°	49.36	49.41	49.47	49.59	49.67	49.74	49.81	49.75
Disorder occupancy	0.86:0.14	0.83:0.17	0.81:0.19	0.79:0.21	0.78:0.22	0.77:0.23	0.76:0.25	0.75:0.25

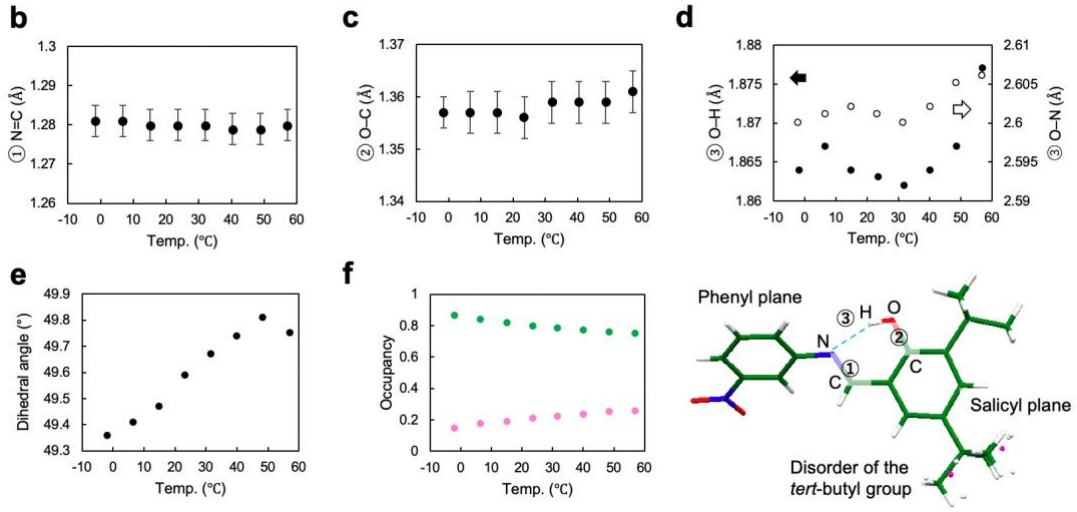

Fig. S4 (a) Temperature dependence of the molecular conformation of the enol-**1** crystal. (b–f) Temperature dependence of the (b) ① N=C, (c) ② O–C, (d) ③ O–H---N and O---N distance, (e) dihedral angle between salicyl and phenyl planes, and (f) disorder occupancy.

a

Temperature/°C	–1.6	6.8	15.2	23.6	32.0	40.4	48.8	57.2
I O---H /Å	2.686	2.691	2.693	2.696	2.699	2.708	2.717	2.711
I O---C /Å	3.309	3.314	3.318	3.322	3.324	3.333	3.34	3.336
I O---H–C /°	125.13	125.09	125.23	125.16	125.28	125.23	125.08	125.27
II H---C /Å	2.852	2.853	2.855	2.862	2.863	2.864	2.868	2.872
II C---C /Å	3.808	3.807	3.807	3.813	3.816	3.815	3.82	3.823
II C---H–C /°	173.21	172.41	172.05	170.78	171.29	170.8	171.28	171.06

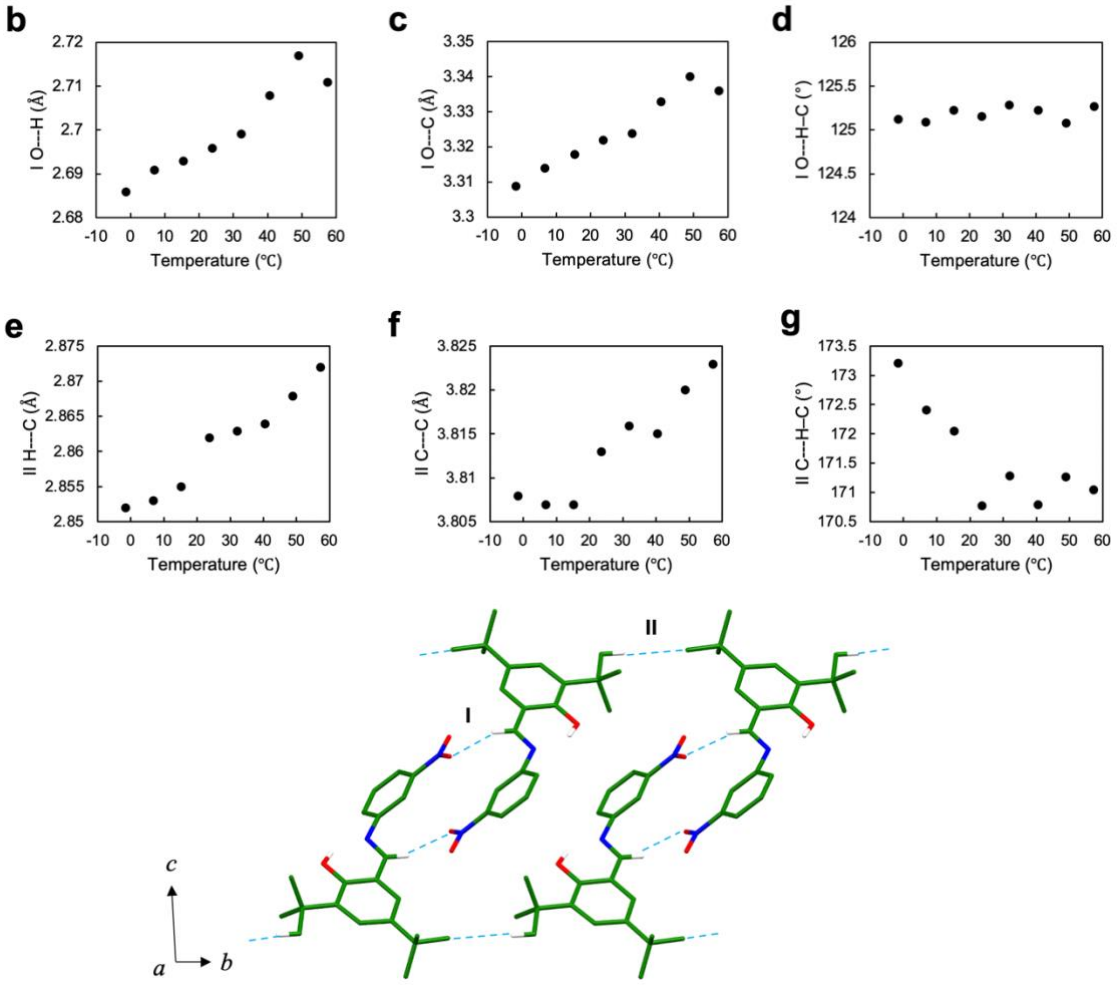

Fig. S5 (a) Temperature dependence of intermolecular interactions of the enol-**1** crystal. (b–g) Temperature dependence of the (b) I O--H distance, (c) I O---C distance, (d) I O---H–C angle (e) II H--C distance, (f) II C---C distance, and (g) II C--H–C angle.

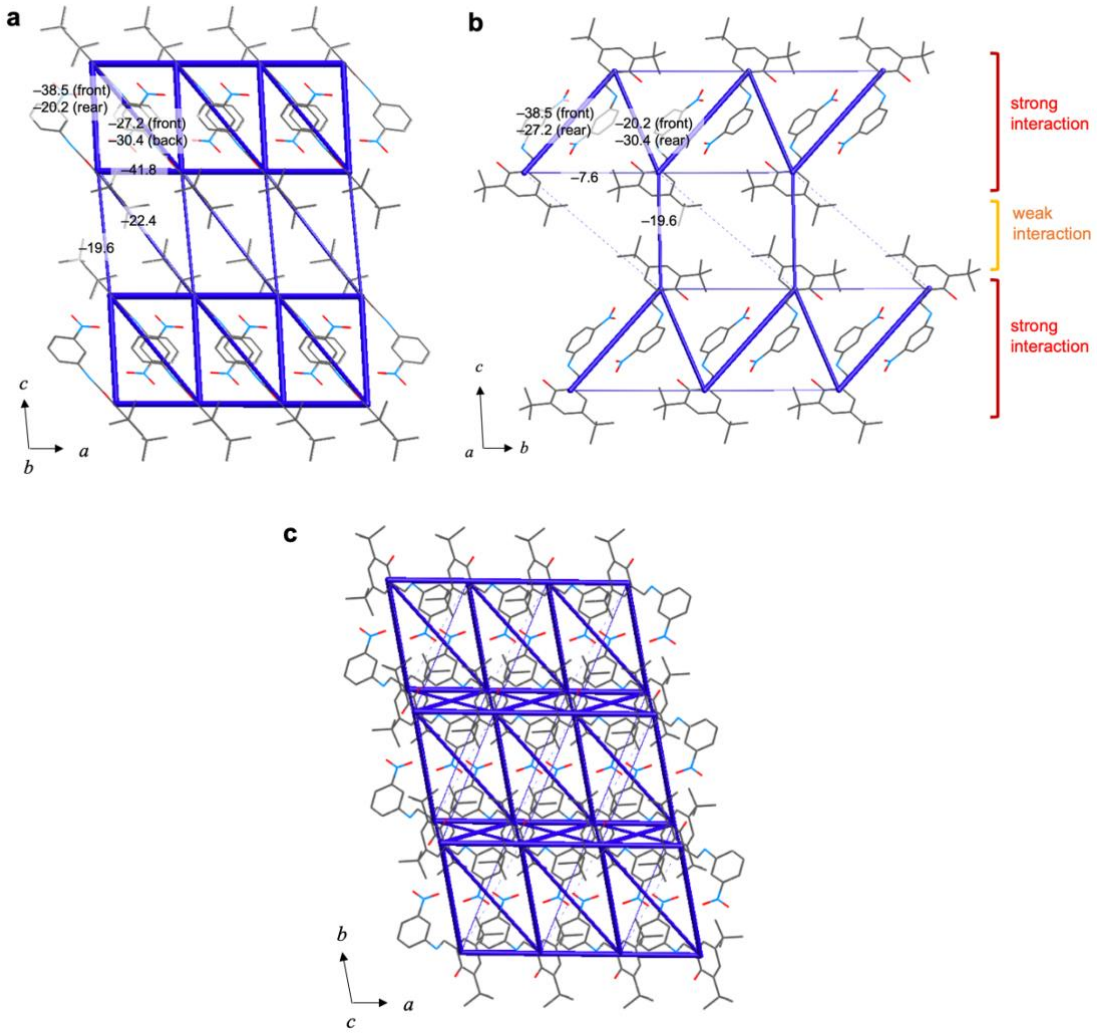

Fig. S6 Energy frameworks viewed from the (a) $(0\bar{1}0)$, (b) (100), and (c) (001) faces at 23.6 °C. The numbers indicate total interaction energies (kJ mol^{-1}).

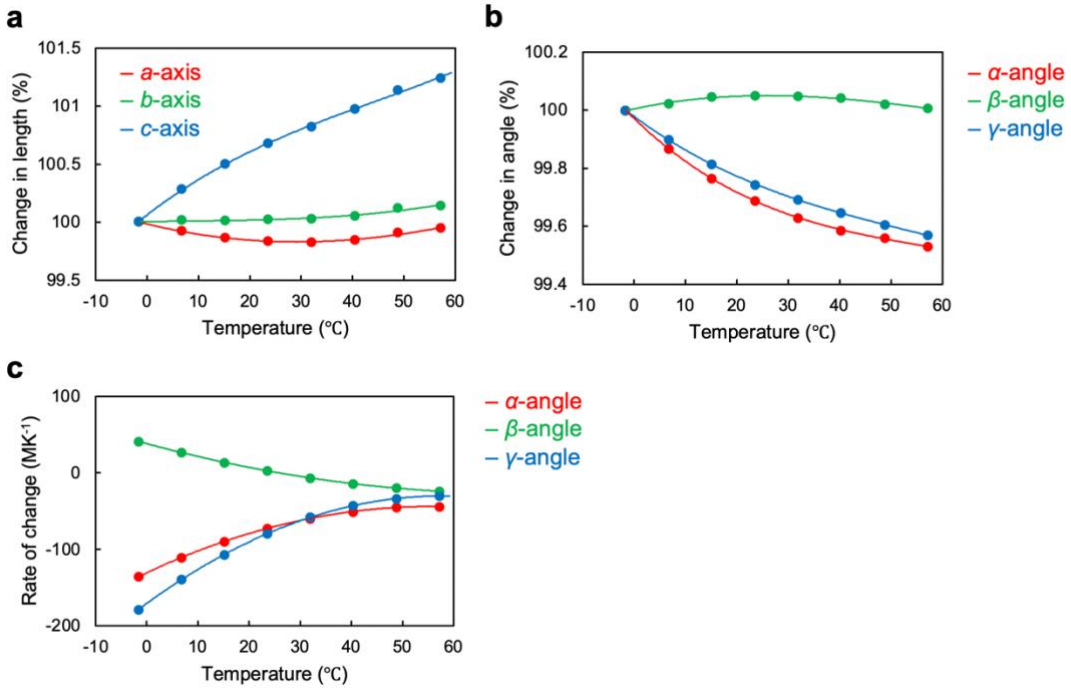

Fig. S7 (a, b) Change of (a) the *a*-, *b*-, and *c*-axes and (b) the *α*-, *β*-, and *γ*-angles relative to −1.6℃. (c) Rate of change of the *α*-, *β*-, and *γ*-angles calculated from the slope of the temperature dependence of the angle in Fig. 2e–g.

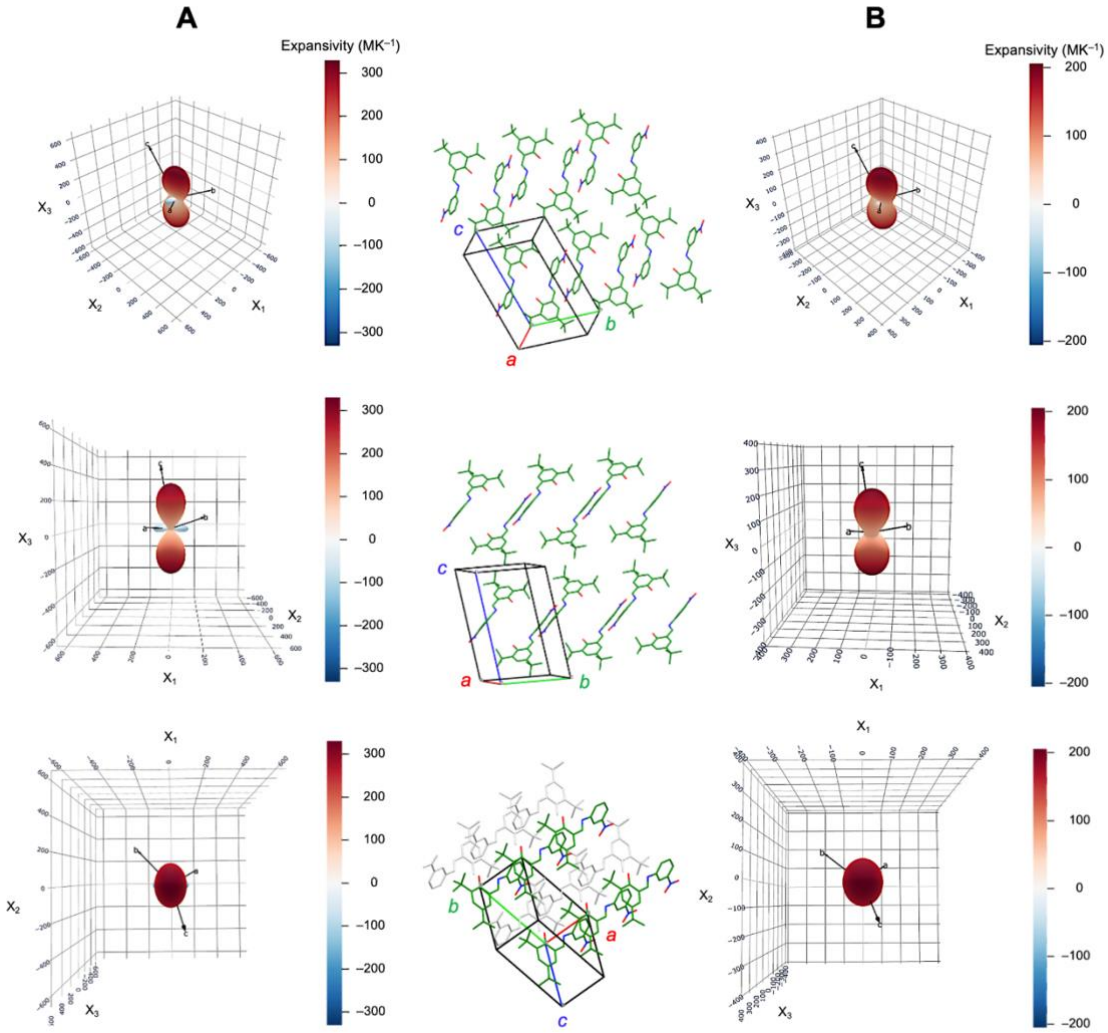

			Direction		
Axes	α (MK^{-1})	σα(MK^{-1})	a	b	c
X_1	-127.7139	8.6398	0.936	-0.35	0.0383
X_2	94.0899	6.4069	0.8111	0.5698	-0.1318
X_3	329.873	16.893	0.4148	0.5811	0.7002
V	295.8453	14.8777			

			Direction		
Axes	α (MK^{-1})	σα(MK^{-1})	a	b	c
X_1	21.0032	4.4008	0.8684	-0.4946	0.0343
X_2	76.5241	1.8882	0.8755	0.4682	-0.1196
X_3	205.3841	6.4741	0.4971	0.5326	0.685
V	303.757	9.2062			

Fig. S8 Expansivity indicatrices obtained from PASCal[S9] in the temperature range (A) from –1.6 to 23.6 °C and (B) from 32.0 to 57.2 °C, molecular packings viewed from the same direction as the expansivity indicatrices, and the principal axes expansion coefficients and volume expansion coefficients. Red and blue represent positive and negative thermal expansion, respectively.

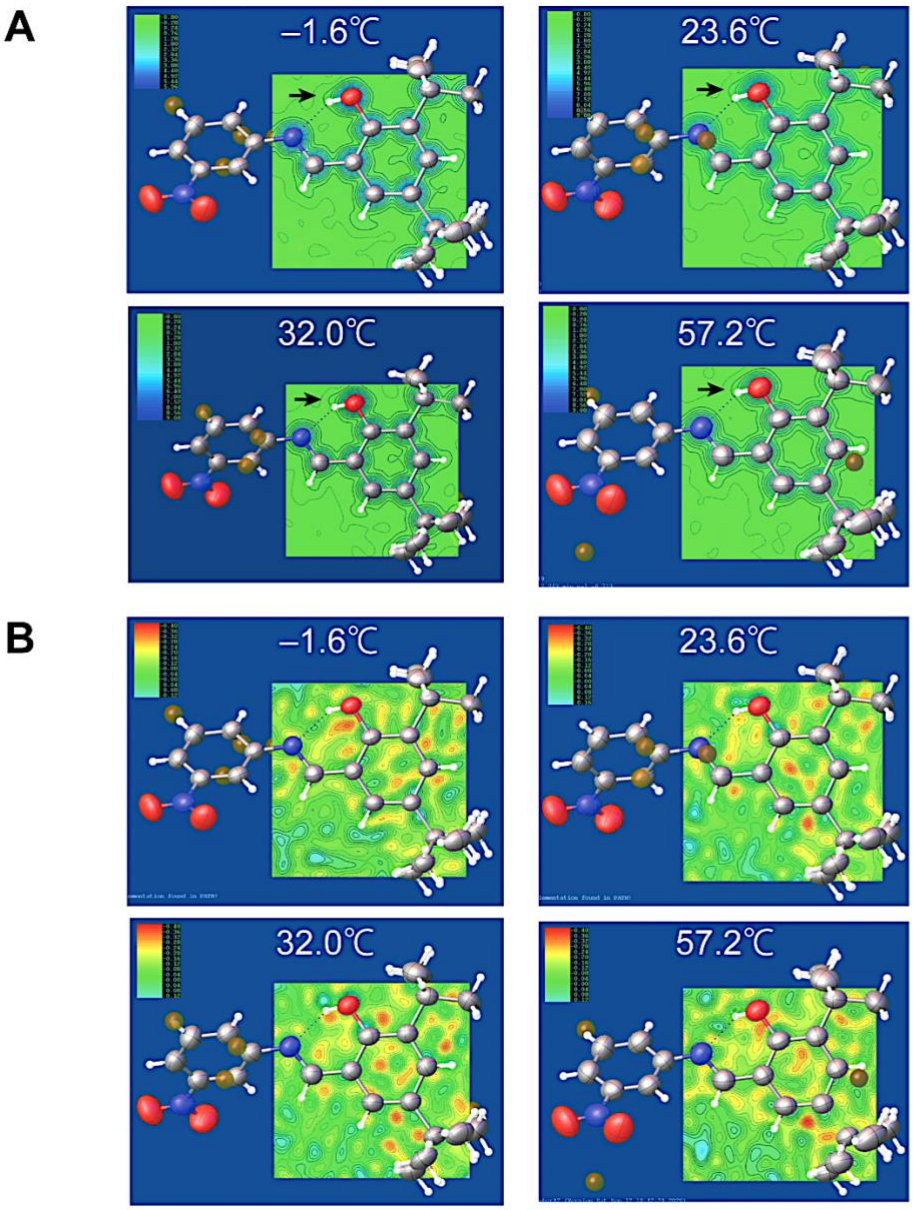

Fig. S9 (A) Fourier maps (F_{obs}) and (B) difference Fourier maps ($F_{obs} - F_{calc}$) of enol-**1** at –1.6, 23.6, 32.0, and 57.2 °C visualised by using Olex2.[S5]

As shown in the Fourier maps (A), the contour intervals around the left side of the oxygen are wide (black arrows) while those around the right side of the oxygen and nitrogen are narrow and concentric, indicating a hydrogen is located around the left side of the oxygen, not nitrogen. As shown in the difference Fourier maps (B), no residue peaks appear around the nitrogen. These results indicate at all temperatures the compound exists as an enol, not a *cis*-keto form, and no proton transfer occurs.

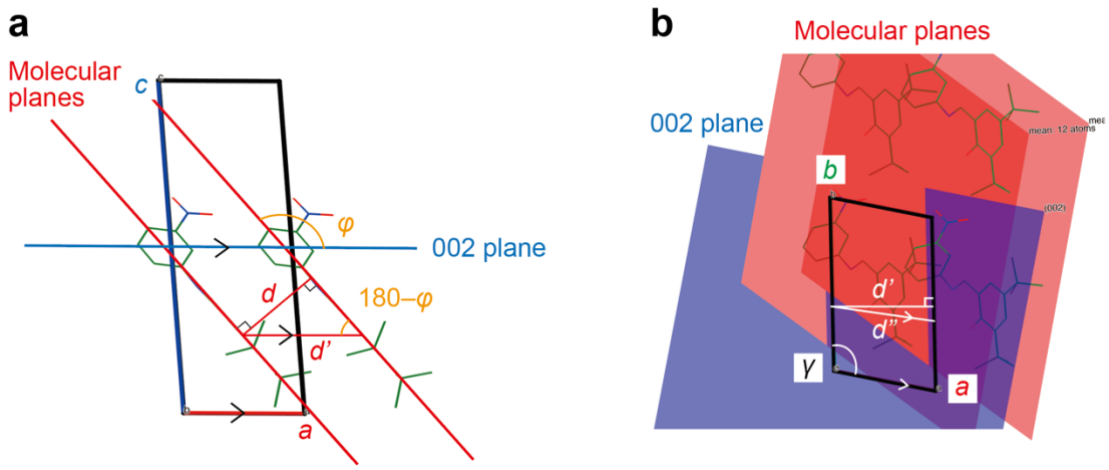

Fig. S10 Schematic illustration of calculation of the *a*-axis length (*d''*) from the interplanar distance (*d*) seen from the (a) $(0\bar{1}0)$ face and (b) (001) face. The equations are as follows:

$$d' = \frac{d}{\sin(180-\varphi)} = \frac{d}{sin\varphi}$$

$$d'' = \frac{d'}{\cos(\gamma-90)} = \frac{d'}{sin\gamma}$$

where *d'* is the distance between two molecular planes along the *a*-axis φ is the tilt angle of the molecular plane against the *a*-axis (or the 002 plane) on the $(0\bar{1}0)$ face.

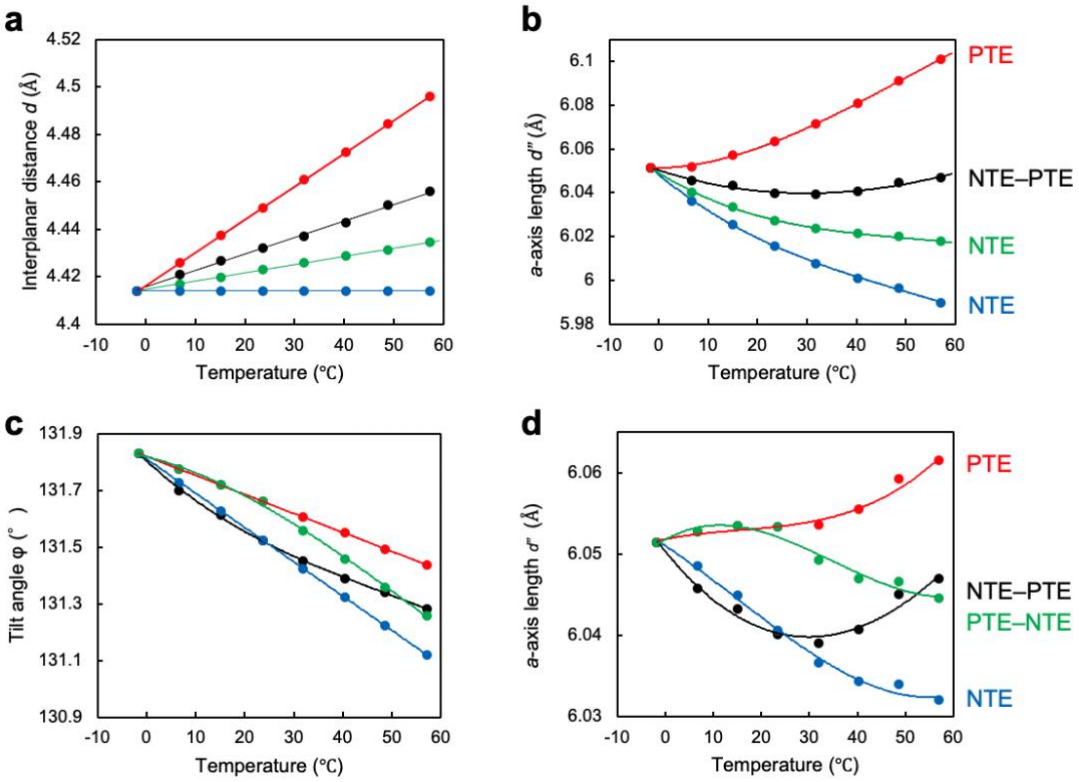

Fig. S11 Calculation of (b, d) the *a*-axis length *d''* with various (a) interplane distance *d* and (c) tilt angle φ, respectively.

(a, b)

black: *d* is experimental values with an increase ratio of 7.0×10^{-4} Å °C^{-1}.

blue: *d* was set to constant (4.414 Å) over the entire temperature range.

green: the increase ratio of *d* is half of the experimental value (3.5×10^{-4} Å °C^{-1}).

red: the increase ratio of *d* is double of the experimental value (1.4×10^{-3} Å °C^{-1}).

Note: φ and γ were experimental values.

(c, d)

black: φ is experimental values, where the decrease ratio of φ is 0.0121 degree °C^{-1} for the low temperature range (–1.6 to 23.6 °C) and 0.0067 degree °C^{-1} for the high temperature range (32.0 to 57.2 °C).

blue: the decrease ratio of φ is 0.0121 degree °C^{-1} over the entire temperature range.

red: the decrease ratio of φ is 0.0067 degree °C^{-1} over the entire temperature range.

green: the decrease ratio of φ is exchanged between low and high temperature ranges, that is, 0.0067 degree °C^{-1} for the low temperature range and 0.0121 degree °C^{-1} for the low temperature range.

Note: *d* and γ were experimental values.

5. Photoisomerisation properties

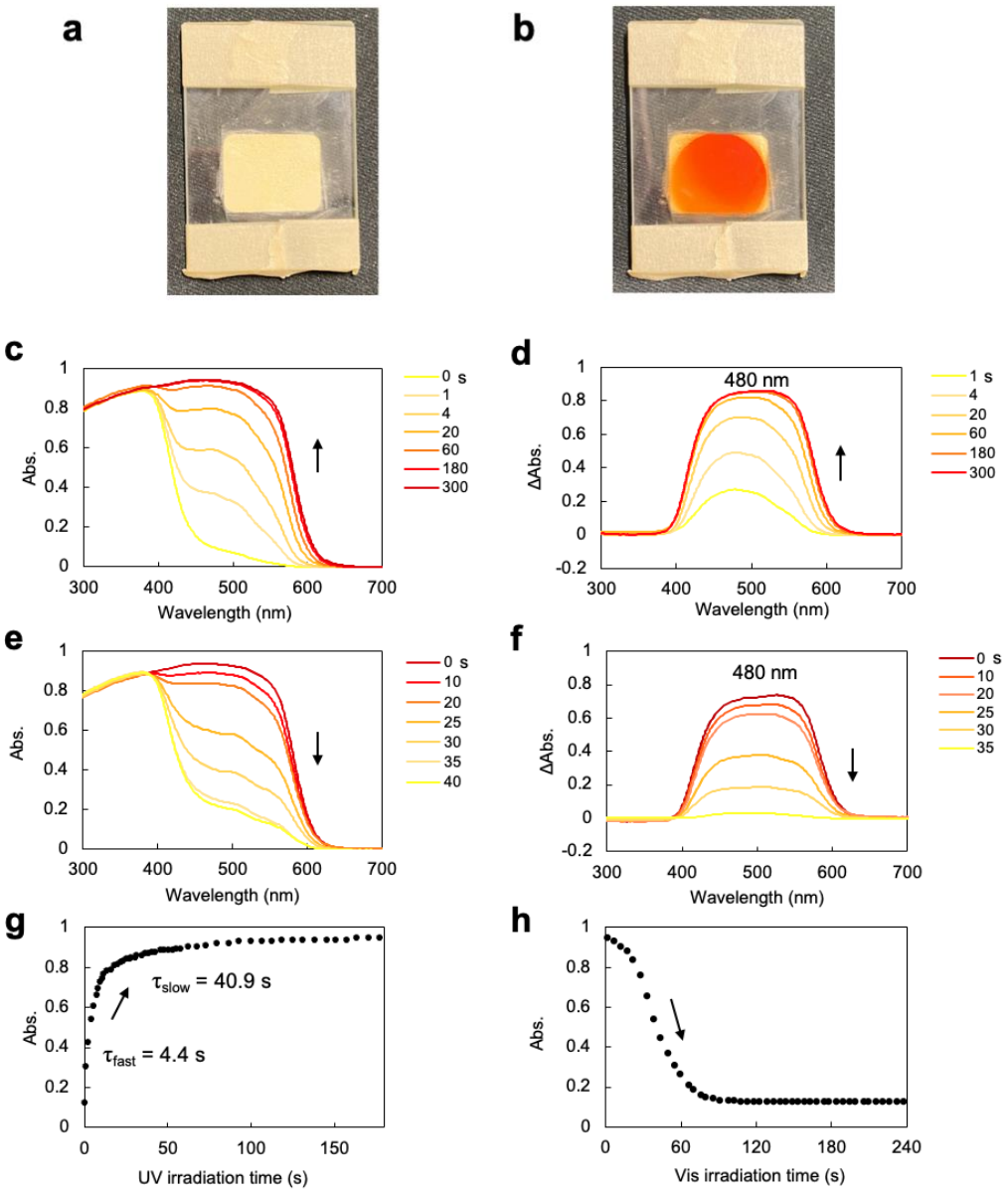

Fig. S12 (a, b) Colour change of powder enol-**1** crystals (a) before and (b) after UV (375 nm; 20 mW cm^{-2}) irradiation for 30 s. (c–f) Ultraviolet–visible (UV–vis) (c, e) diffuse reflectance spectra and (d, f) diffuse reflectance difference spectra of powder enol-**1** crystals (a, c) upon UV laser (375 nm; 20 mW cm^{-2}) and (d, f) visible laser (520 nm; 20 mW cm^{-2}) irradiation. (g, h) Time dependence of the absorption of powder enol-**1** crystals at 480 nm. (g) UV laser (375 nm; 46 mW cm^{-2}) irradiation. (h) Visible laser (375 nm; 20 mW cm^{-2}) irradiation.

6. Photoactuation

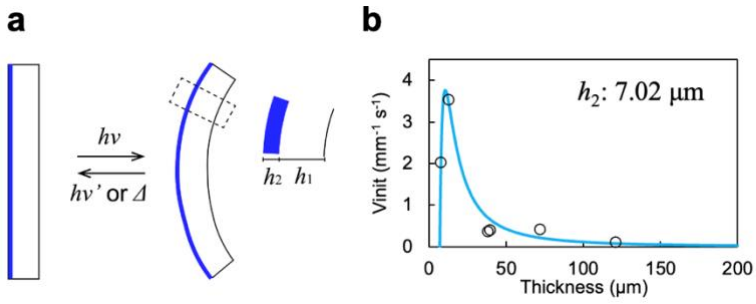

Thickness (μm)	Vinit (mm^{-1} s^{-1})
7.8	2.04
12.9	3.55
38.1	0.36
39.4	0.41
72.0	0.43
121	0.12

c

Crystal	Irradiated face	h_2 /μm	UV wave-length /nm	UV intensity /mW cm^{-2}	Reference
1	(001)/(00-1)	7.02	375	1,280	This work
2	(001)/(00-1)	2.64	365	1,300	[S13]
3	(100)/(-100)	3.54	375	928	[S14]

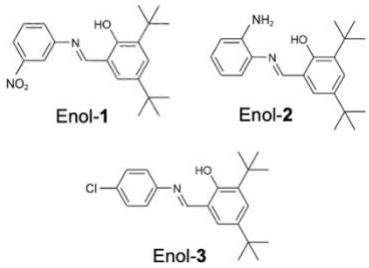

Fig. S13 Estimation of the photo-reacted layer thickness (h_2) upon UV laser irradiation (375 nm; 1280 mW cm^{-2}) by Timoshenko's bimetal model.[S10–12] (a) Schematic illustration of the Timoshenko's bimetal model. (b) Thickness dependence of the initial speed (V_{init}) of the curvature change of the enol-**1** crystal by photoisomerisation alone. Open black dots are measured values, and the blue solid line is fitting curve calculated by the bimetal model. h_2 was estimated to be 7.02 μm. (c) Comparison of h_2 with crystals of other salicylideneaniline derivatives. UV light penetrates the enol-**1** crystal deeper than enol-**2**[S13] and enol-**3** crystals[S14].

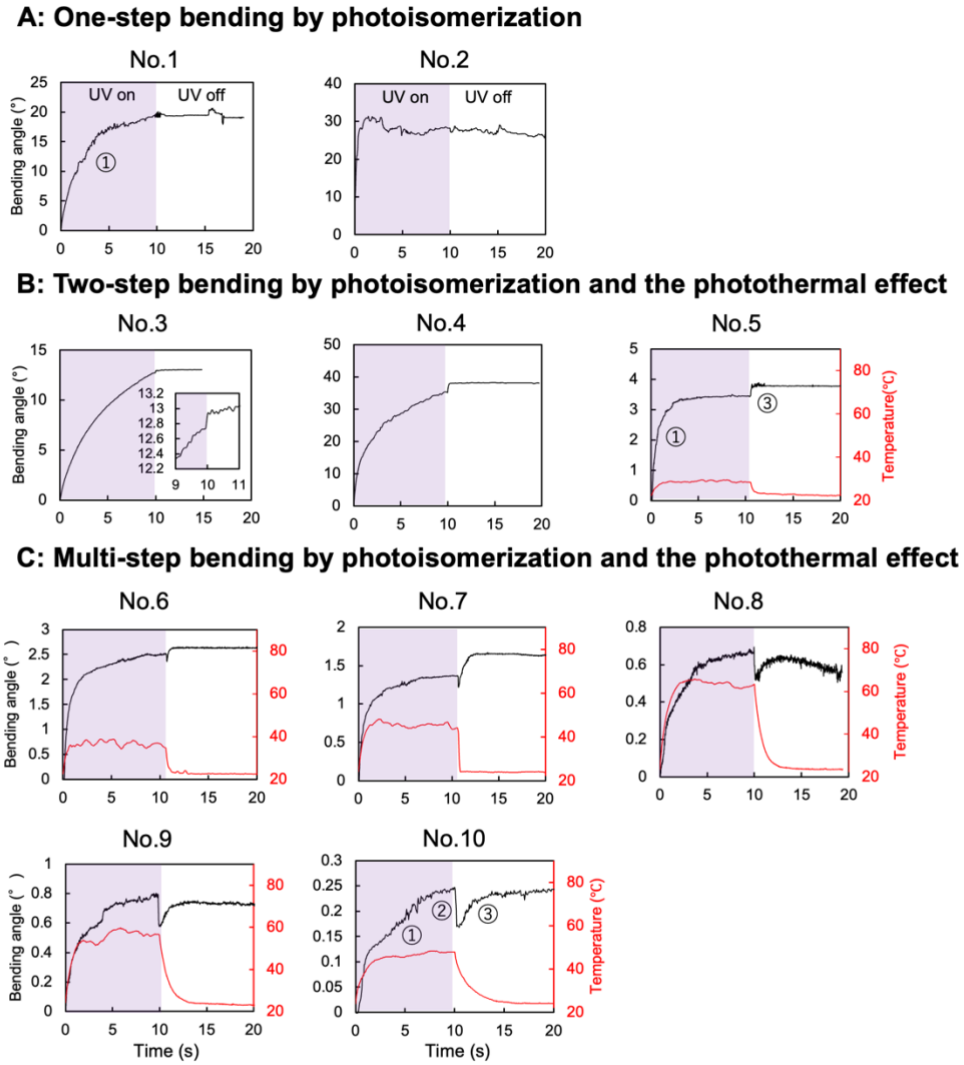

No.	Size (μm³) Length	Width	Thickness	Aspect ratio (Length/ Thickness)	Volume (mm³ ×10⁻³)	Maximum bend angle (°) ① [a]	② [b]	③ [c]	Time constant (s) Photoisomerization ①–1 [d]	①– 2 [d]	③ [e]
1	281	97.0	7.8	36.0	0.21	19.4			0.26	2.45	
2	3270	16.2	12.9	253	0.68	31.4			0.24	2.10	
3	631	59.7	38.1	16.6	1.44	12.7		0.32	0.85	6.86	0.05
4	4450	53.3	39.4	113	9.35	35.3		2.90	0.37	5.09	0.09
5	1020	89.0	72.0	14.2	6.54	3.49		0.44	0.52	1.76	0.04
6	2000	212	121	16.5	51.3	2.52	-0.16	0.30	0.55	6.11	0.14
7	2410	243	166	14.5	97.2	1.37	-0.15	0.46	0.43	3.28	0.51
8	2470	347	216	11.4	185	0.79	-0.33	0.19	0.22	1.78	0.70
9	2560	361	244	10.5	225	0.80	-0.20	0.17	0.26	3.15	0.65
10	4593	505	305	15.1	707	0.25	-0.08	0.07	0.80	9.73	1.41

Fig. S14 Summary of the bending behaviour of enol-**1** crystals upon UV laser (375 nm; No.1–9: 1280 $mWcm^{-2}$, No.10: 317 $mWcm^{-2}$) irradiation. A: One-step bending by photoisomerisation. B: Two-step bending by photoisomerisation and the photothermal effect. C: Multistep bending by photoisomerisation and the photothermal effect.

(continued)

[a] Bending away through photoisomerisation upon UV laser irradiation.
[b] Bending toward through relaxation of the photothermal effect upon removal of UV laser.
[c] Bending away through relaxation of the photothermal effect upon removal of UV laser.
[d] Time constants for bending by photoisomerisation.
[e] Time constants for bending away through relaxation of the photothermal effect upon removal of UV laser.

Note on the top surface measurements: the infrared thermography camera could not measure the irradiated top surface temperatures of crystals No.1–4 because their top surfaces are too narrow (<60 μm) to measure.

Note on the calculation of time constants: the time constants for bending by photoisomerisation (τ_{fast} and τ_{slow}) were calculated by fitting the time dependence of the bending angle with the following biexponential curve:

$$\theta(t) = \sum_{i=fast,\ slow} A_i \left\{1 - \exp\left(\frac{-t}{\tau_i}\right)\right\}$$

where θ is the bending angle, t is the UV irradiation time, A is the constant, and τ is the time constant.

The time constants for bending away through relaxation of the photothermal effect were calculated by fitting the time dependence of the bending angle with the following monoexponential curve:

$$\theta(t) = A\left\{1 - exp(\frac{-t}{\tau})\right\} + B$$

where θ is the bending angle, t is the time after the crystal bends away again, A and B are constants, and τ is the time constant.

Note on the fitting of bending through photoisomerisation: unlike photoisomerisation-driven bending of other salicylideneaniline crystals,[S13,S14] the time dependence of the bending angle cannot be fitted by a monoexponential curve with one time constant (see Fig. S21). One possible reason is that the enol to *trans*-keto photoisomerisation of the enol-**1** crystal is not a normal first-order reaction but an autocatalytic one. Indeed, absorbance of powder enol-**1** crystals increased as a biexponential curve upon UV irradiation (Fig. S12g) and returned as a sigmoid curve upon visible light irradiation (Fig. S12h), indicating that at least photochemical back-isomerisation from the *trans*-keto to enol form would be an autocatalytic reaction.[S15]

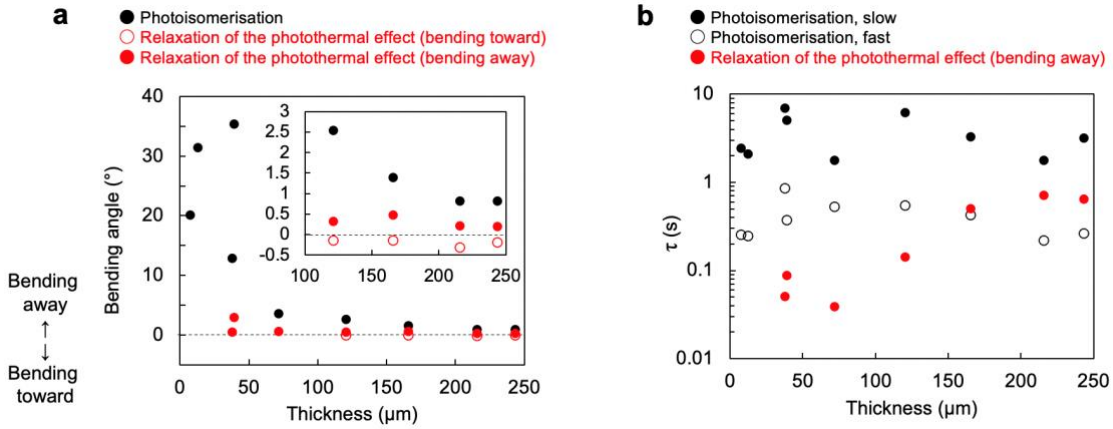

Fig. S15 Thickness dependence of the (a) maximum bending angle and (b) time constants for the bending and straightening of enol-**1** crystals upon UV laser irradiation (375 nm; 1280 mWcm^{-2}).

Note on the relationship between crystal size time constants: the time constants of bending away by the relaxation of the photothermal effect (red circles in Fig. S15b) increased in proportion to the thickness. This would be because the thicker the crystal is the longer it takes to the temperature gradient along the thickness direction becomes zero by cooling. In contrast, no significant correlation between the thickness and the time constants for photoisomerisation (black solid and open circles in Fig. S15b) contrary to other salicylideneaniline crystals that the time constants increase in proportion to the thickness.[S13,S14] One possible reason is that these time constants were calculated from the bending upon UV irradiation for 10 s (Fig. S14) but the bending did not finish completely in 10 s. Indeed, an enol-**1** crystal kept bending even after 120 s (Fig. S21). Given that thin crystals (No.1, 2 in Fig. S14) bent completely in 10 s but thick crystals did not (No.3–10 in Fig. S14), we can expect the bending by photoisomerisation would be slower for thicker crystals, as in previous reports.[S13,S14]

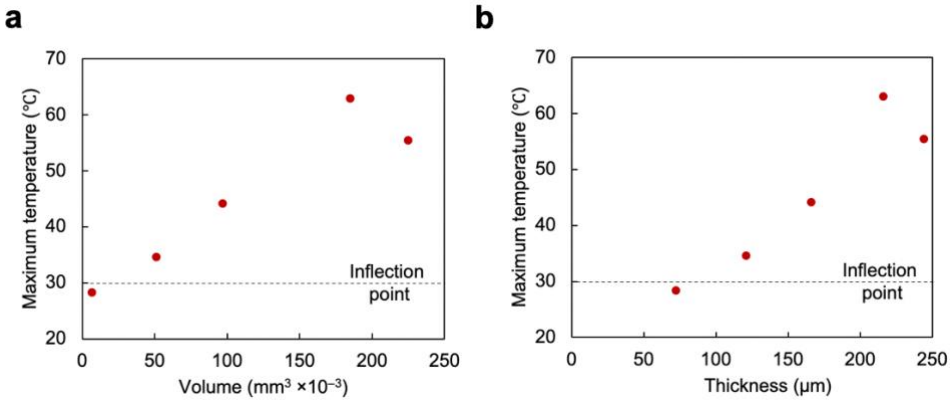

Fig. S16 (a) Thickness and (b) volume dependence of the maximum top surface temperature upon UV laser irradiation (375 nm; 1280 $mWcm^{-2}$) for 10 s. The maximum temperature increased in proportion to the thickness and volume.

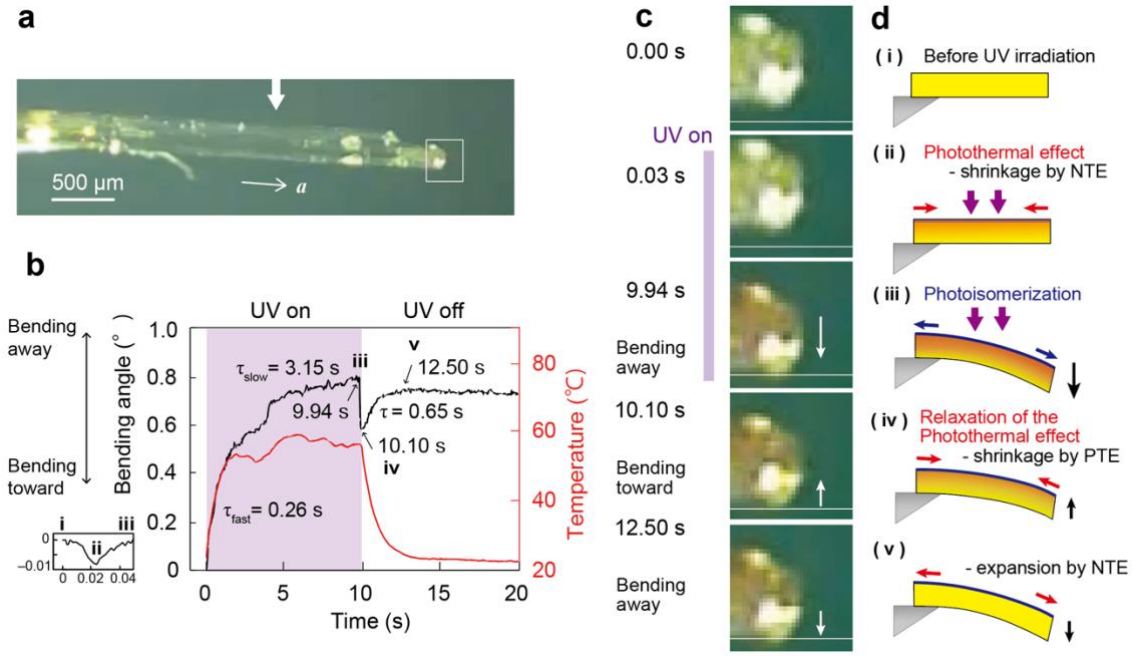

Fig. S17 Multistep bending of a thick enol-**1** crystal (2560×361×244 μm^3, No.9 in Fig. S14) upon UV laser irradiation (Movie S1). (a) Photo of the crystal. (b) Time dependence of the bending angle. (c) Sequential snapshots of the right rip of the crystal. (d) Schematic illustration of the bending mechanism.

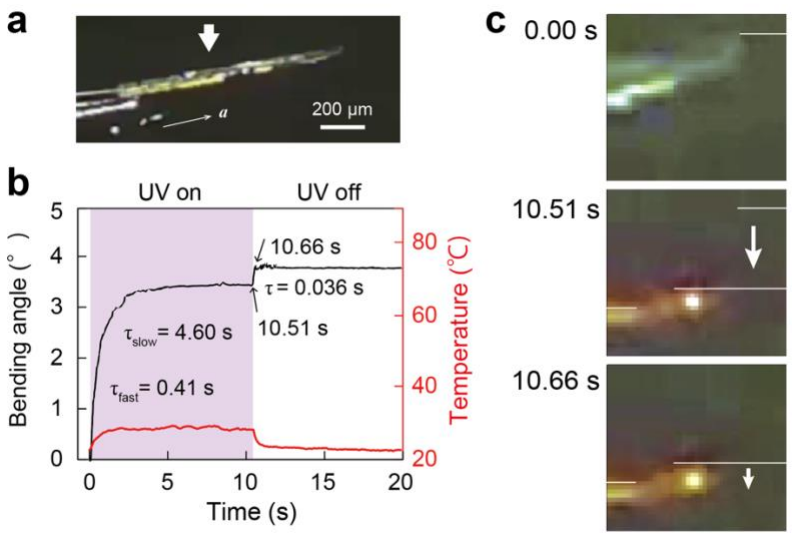

Fig. S18 Two-step bending of a slightly thick enol-**1** crystal (1020×89.0×72.0 μm^3, No.5 in Fig. S14) upon UV laser irradiation (Movie S2). (a) Photo of the crystal. (b) Time dependence of the bending angle (black) and maximum top surface temperature (red). (c) Sequential snapshots of the right tip of the crystal.

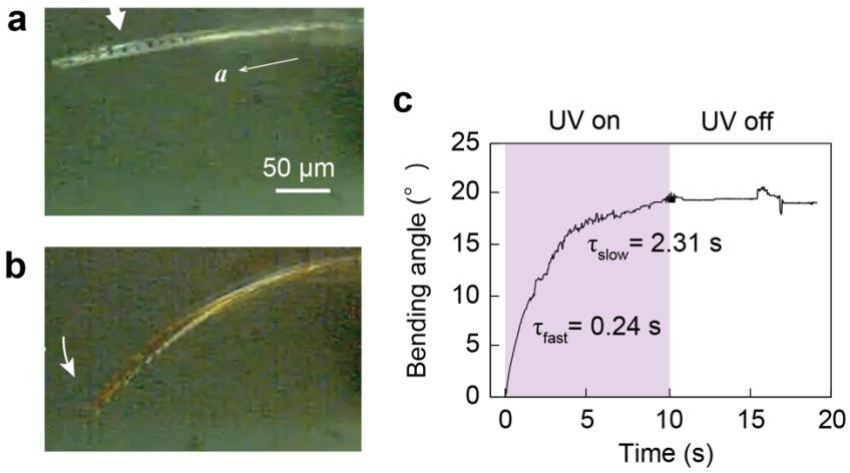

Fig. S19 Bending of a thin enol-**1** crystal (281×97.0×7.8 μm^3, No.1 in Fig. S14) upon UV laser irradiation (Movie S3). (a, b) Photos of the crystal (a) before and (b) under UV irradiation for 10 s. (c) Time dependence of the bending angle.

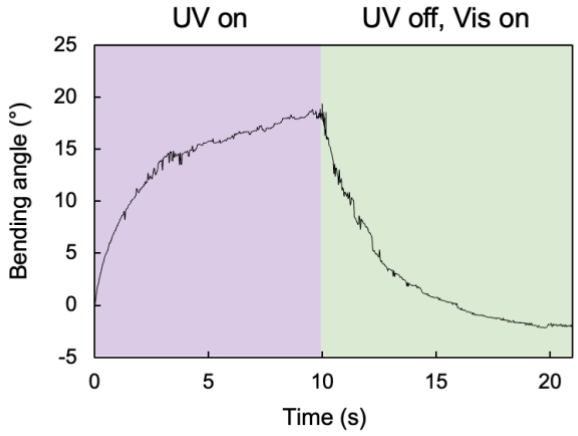

Fig. S20 Reversible bending of a thin enol-**1** crystal (281×97.0×7.8 μm^3, No.1 in Fig. S14) upon UV laser irradiation for 10 s and subsequent visible laser (520 nm) irradiation.

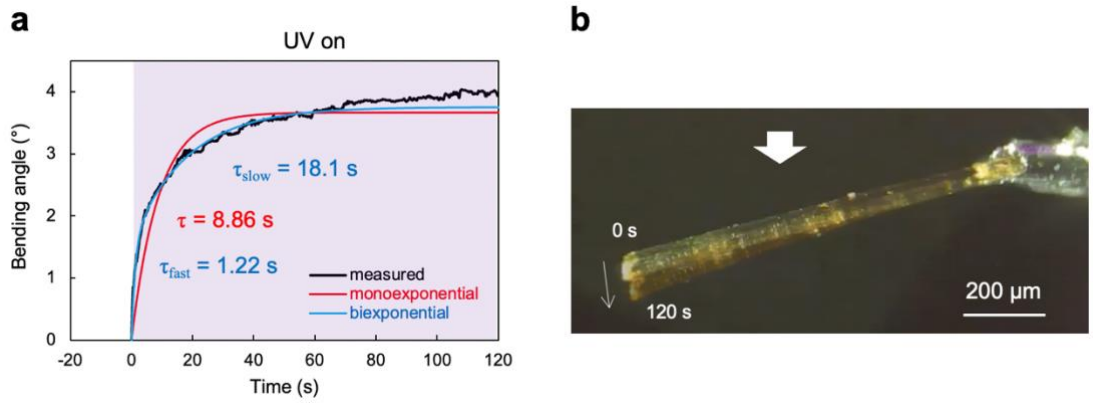

Fig. S21 Bending of an enol-**1** crystal (955.2×148.6×51.3 μm^3) upon UV irradiation (365 nm; 1300 mWcm^{-2}) for 120 s. (a) Time dependence of the bending angle and monoexponential and biexponential curves. (b) Photographs of the crystal before (0 s) and under UV light irradiation (120 s).

7. List of movies

Movie S1:

multistep bending of a thick enol-**1** crystal (2560×361×244 μm^3) through photoisomerisation and the photothermal effect upon UV laser (375 nm; 1280 mW cm^{-2}; 9.94 s) irradiation on the (001)/(00$\bar{1}$) top face from the top (realtime) (MP4)

Movie S2:

two-step bending of a slightly thick enol-**1** crystal (1020×89.0×72.0 μm^3) through photoisomerisation and the photothermal effect upon UV laser (375 nm; 1280 mW cm^{-2}; 10.51 s) irradiation on the (001)/(00$\bar{1}$) top face from the top (realtime) (MP4)

Movie S3:

bending of a thin enol-**1** crystal (281×97.0×7.8 μm^3) through photoisomerisation upon UV laser (375 nm; 1280 mW cm^{-2}; 10 s) irradiation on the (001)/(00$\bar{1}$) top face from the top (realtime) (MP4)

Movie S4:

Actuation switching of a thick enol-**1** crystal (4590×505×317 μm^3) by temperature upon UV laser (375 nm; 317 mW cm^{-2}; 10 s) irradiation on the (001)/(00$\bar{1}$) top face from the top (realtime) (MP4)

8. References

1. AIST Thermophysical Properties Database System, 'https://tpds.db.aist.go.jp/tpds-web/index.aspx?MaterialID=11138' Access: 2022/07/29
2. G. M. Sheldrick, *Acta Crystallogr., Sect. A: Found. Adv.* **2015**, *71*, 3–8.
3. G. M. Sheldrick, *Acta Crystallogr., Sect. C: Struct. Chem.* **2015**, *71*, 3–8.
4. CrystalStructure, version 4.2.2.; Rigaku Corporation: Tokyo, Japan, 2016.
5. O. V. Dolomanov, L. J. Bourhis, R. J. Gildea, J. A. K. Howard, H. Puschmann, *J. Appl. Cryst.* **2009**, *42*, 339–341.
6. P. R. Spackman, M. J. Turner, J. J. McKinnon, S. K. Wolff, D. J. Grimwood, D. Jayatilaka, M. A. Spackman, *J. Appl. Cryst.* **2021**, *54*, 1006–1011.
7. D. Brown, Tracker Video Analysis and Modeling Tool, version 5.1.2., Cabrillo College, Aptos, California, USA, 2019.
8. T. Kawato, H. Koyama, H. Kanatomi, M. Isshiki, *J. Photochem.*, **1985**, *28*, 103–110.
9. M. Lertkiattrakul, M. L. Evans, M. J. Cliffe, *J. open source softw.*, **2023**, *8*, 5556.
10. S. Timoshenko, *J. Opt. Soc. Am.* **1925**, *11*, 233−255.
11. D. Kitagawa, S. Kobatake, *J. Phys. Chem. C* **2013**, *117*, 20887–20892.
12. D. Kitagawa, C. Iwaihara, H. Nishi, S. Kobatake, *Crystals* **2015**, *5*, 551–561.
13. S. Hasebe, Y. Hagiwara, J. Komiya, M. Ryu, H. Fujisawa, J. Morikawa, T. Katayama, D. Yamanaka, A. Furube, H. Sato, T. Asahi, H. Koshima, *J. Am. Chem. Soc.* **2021**, *143*, 8866–8877.
14. S. Hasebe, Y. Hagiwara, K. Hirata, T. Asahi, H. Koshima, *Mater. Adv.* **2022**, *3*, 7098–7106.
15. F. Tong, M. P Hanson, C. J. Bardeen, *Phys. Chem. Chem. Phys.*, **2016**, *18*, 31936–31945.